RESEARCH ARTICLE

# Time-resolved volumetric particle tracking velocimetry of large-scale vortex structures from the reattachment region of a laminar separation bubble to the wake

E. Wolf · C. J. Kähler · D. R. Troolin ·
C. Kykal · W. Lai

**Abstract** The present paper presents time-resolved volumetric Particle Tracking Velocimetry measurements in a water towing tank on a SD7003 airfoil, performed at a Reynolds number of 60,000 and a 4° angle of attack. The SD7003 airfoil was chosen because of its long mid-chord and stable laminar separation bubble (LSB), occurring on the suction side of the airfoil at low Reynolds numbers. The present study focuses on the temporal resolution of unsteady large-scale vortex structures emitted from the LSB. In contrast to other studies, where only the observation of the flow in the transition region was examined, the entire flow from the leading edge to the far wake of the airfoil was investigated here.

## 1 Introduction

A laminar separation bubble is a typical low Reynolds number phenomenon, which occurs on slender airfoils, as investigated in turbine blades, sailplanes or drones. An adverse pressure gradient (APG) causes the laminar flow to separate from the surface and Tollmien-Schlichting (T-S) waves develop and trigger Kelvin-Helmholtz (K-H) instabilities in the shear layer above the separated region due to inertial disturbances in the free-stream. This results in an unsteady flow state (visible in form of Reynolds stresses) and results in a reattachment of the apparently turbulent shear layer (see Fig. 1). As the size of the bubble has a non-linear dependency on $\alpha$, slight changes in $\alpha$ may result in a sudden enlargement of the bubble or even a separated shear layer that never reattaches causing a broad loss of lift. Besides the technical relevance of this phenomenon on engine and sailplane designs, this problem is also appealing to the fundamental point of view as a number of important fluid mechanical effects, such as separation, transition and turbulence, can be examined simultaneously on a small scale.

Gaster (1966) developed a model of a 2D steady LSB and investigated the dependency on the APG, which led him to critical values that can cause a sudden "bursting" of the bubble if exceeded. Furthermore, Horton (1968) picked up these results and analyzed the influence of the Reynolds number as well. He found differences between short and long separation bubbles like the fact that short bubbles have a much smaller and locally limited influence on the pressure distribution than long ones. Ol et al. (2005) compared the results measured in three different low turbulence flow facilities at Reynolds number 60,000 to show the influence of the turbulence intensity on the transition and reattachment on the SD7003 airfoil. Figure 1 shows the distribution of mean velocity and Reynolds stresses measured in the Braunschweig University of Technology's wind tunnel at $\alpha = 4°$, where one can observe the mean locations of separation, transition and reattachment.

E. Wolf (✉) · C. J. Kähler
Institute for Fluidmechanics and Aerodynamics,
University of German Armed Forces Munich,
Werner-Heisenberg-Weg 39, 85577 Neubiberg, Germany
e-mail: erik.wolf@drsnet.de

C. J. Kähler
e-mail: christian.kaehler@unibw.de

D. R. Troolin · W. Lai
TSI Incorporated, 500 Cardigan Road,
Shoreview, MN 55126, USA
e-mail: dan.troolin@tsi.com

W. Lai
e-mail: wing.lai@tsi.com

C. Kykal
TSI GmbH, Neuköllner Strasse 4, 52068 Aachen, Germany
e-mail: carsten.kykal@tsi.com

**Fig. 1** Mean velocity (*top*) and Reynolds stresses (*bottom*) measured with PIV on the SD7003 airfoil at $\alpha = 4°$ and $Re = 60{,}000$ (Ol et al. 2005)
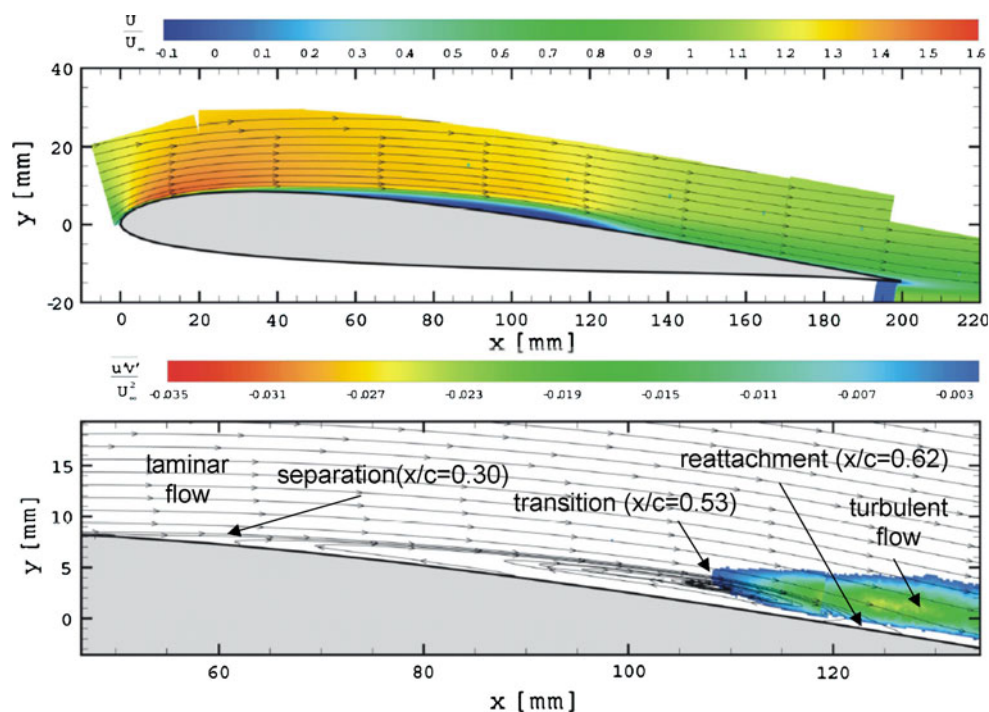
However, as previously mentioned, the LSB is very sensitive to the boundary conditions (turbulence level) and thus highly unsteady. Pauley et al. (1990) performed numerical investigations on the unsteady nature of the bubble. They created an external APG and studied the separation behavior of a two-dimensional laminar boundary layer flow and found out that a high APG leads to a periodic vortex shedding from the LSB. Furthermore, they also suggested that Gaster's (1966) 'bubble-bursting' corresponds to a time-averaged vortex shedding. Later, Spalart and Strelets (2000) performed a direct numerical simulation (DNS) of an LSB on a flat plate where they were able to detect a low-frequency oscillation of the separated shear layer known as "flapping" of the bubble. Due to the fact that small disturbances in the incoming flow did not change in the simulations, compared to experimental findings, they suggested that K-H waves in the separated shear layer are responsible for the transition. Similarly, Yang and Voke (2001) discussed the K-H instability mechanism after their large eddy simulation (LES) of flow on a flat plate. Using the time-resolved-PIV technique, Hain and Kähler (2005) discussed the T-S waves growing in the separated shear layer and their relationship with the "flapping". Watmuff (1999) detected the K-H wave packets by means of hotwire anemometry, providing 3D vortex loops at the downstream end of the separation bubble. Zhang et al. (2008) mapped K-H vortex structures and verified that they are responsible for the transition in an LSB. Thereby, they detected Λ-shape vortex structures rising from the transition region. This also corresponded with 3D DNS

calculations by Alam and Sandham (2000), who had found out that the Λ-vortices induce the breakdown to turbulence. Zhang et al. (2008) were able to track these structures being shed and propagating downstream, but not changing their identity nor substantially decreasing in strength. Using scanning PIV, Burgmann and Schröder (2008) and Burgmann et al. (2007) also focused on the phenomenology of these shed vortices. They detected the presence of primary C-shape vortices, separating periodically from the main recirculation region and moving further downstream. The C-shape vortex is characterized by a distinctive backflow region, which was also observed by Hain and Kähler (2005). Additionally, they depicted secondary 'screwdriver' vortices with a streamwise orientation as well as arc-like vortex structures emerging further downstream. Burgmann and Schröder (2008) proposed a correspondence of these vortex structures to the K-H-induced shear layer roll-ups. Due to the three-dimensional non-stationary nature of the complex vortex structures, time-resolved investigations with a real 3D measurement system are desirable to characterize the topology of the structures and their development, decay and interaction. Therefore, the PTV technique, called V3V, was used in a low turbulence water towing tank to characterize the natural transition process in space and time. The water towing tank was used for two reasons: (1) to minimize its turbulence level, as the freestream turbulence affects the transition quite strongly and (2) to avoid the boundary layer effects at the side-walls of wind tunnels, which accelerate the flow over the airfoil and thus stabilize the transition process in an unnatural way.

Besides the transition process, the influence of the tip-vortex, which is unavoidable in towing tank experiments, was systematically studied by changing the gap between the tank's bottom surface and the airfoil's tip for two reasons: (1) a gap flow between the airfoil and the side-wall of the towing tank may result in a perturbation on the entire flow field of the airfoil. Therefore, it has to be investigated whether or not the flow is two-dimensional and the effect of the center of the airfoil on the transition process is negligible so that no cross-flow instability occurs. (2) As the streamwise motion in the corner-vortex is reduced, the free-stream flow around the airfoil is accelerated due to continuity. This results in a larger Reynolds number and other transition properties that are of high significance for the present investigation. Therefore, it is essential to show that this effect is negligible. The transition examination shows that three-dimensional coherent vortex structures shed near the reattachment region.

## 2 Experimental setup

### 2.1 V3V technique

Volumetric 3-Component Velocimetry (V3V) is a photogrammetric laser and camera-based technique licensed and refined by TSI incorporated and based on the original defocused digital Particle Image Velocimetry (DDPIV) concept of Willert and Gharib (1992) and Pereira et al. (2000) to obtain fluid velocity vectors over a relatively large volume ($12 \times 12 \times 10$ cm$^3$ in the current experiments) at a single instant in time. A compact camera probe consisting of three apertures (each with a 4-million-pixel CCD array and pixel size of 7.4 microns) with three 50 mm lenses at f#16 arranged in a triangular configuration and separated by 17 cm was utilized to record the $X$, $Y$ and $Z$ locations of laser-illuminated tracer particles suspended in the fluid at two instants separated by a short time ($\Delta t$). The camera was located at a distance of 771 mm from the center of the measurement volume, for a maximum viewing angle of approximately 10°. A calibration was performed by traversing a target with a known dot spacing of 5 mm through the measurement volume and capturing images at regular intervals of 5 mm. The alignment of the camera's target was achieved through the use of a laser alignment diode, mounted at the center of the camera and oriented perpendicular to the camera face. An automated traverse, which was used to move the target to each measurement plane, was run through the full span of the measurement volume. It was confirmed that the position of the laser spot on the center of the target did not change more than approximately 0.25 mm over the span of the entire measurement volume. The position of the camera

relative to the tank was confirmed by aligning the laser such that the reflection of the beam off the surface of the glass was coincident with the incoming beam. The calibration consists of a set of polynomial-fit equations that relate the optical location of the calibration dot cloud to the three sensors, through the concept of "triplets". The in situ calibration corrects for image distortion (such as barrel lens distortion) and optical aberrations (such as astigmatisms due to viewing across the air/glass/water interface). At the reference plane (defined as the plane where the images from the three apertures are coincident), a single particle lies at the same $X$ and $Y$ location on each camera sensor. For planes, forward of the reference plane, a single particle appears at a slightly different location on each camera sensor, and if the three images were overlaid, the pattern formed would be a triangle. The term "triplet" refers to this unique triangular pattern, which is different for every $Z$-location in the volume. Figure 2 shows the triplet pattern for multiple discrete planes throughout the measurement volume. Smaller triplets represent planes closer to the reference plane. Data processing consisted of four steps. The first was the particle identification, which is performed separately for each of the 6 images (two images from each sensor). Particles were identified based on an intensity threshold and size. The typical number of 2D particle images identified in each image was approximately 100,000. The next step was the triplet identification, whereby each particle in the 2D images was scanned according to the calibration to find potential triplet matches from the other two apertures. A schematic of this three-step process is shown in Fig. 3. In this example, a particle is identified in the top image. Due to the unique shape of the triplet, the search begins within a predefined path for a matching particle from the right image (labeled as "Coarse Search" in the figure). Particles matching the coarse search criteria must fit the calibration polynomial to within 1
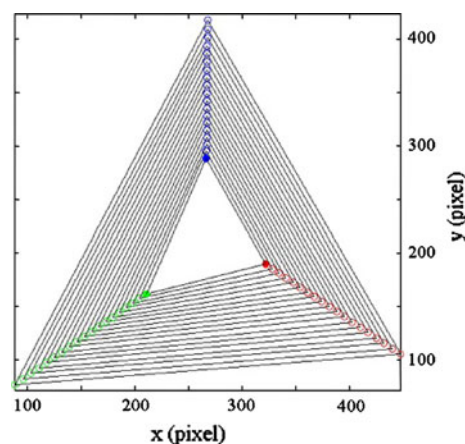


**Fig. 2** Calibration triplets at multiple planes through the measurement volume
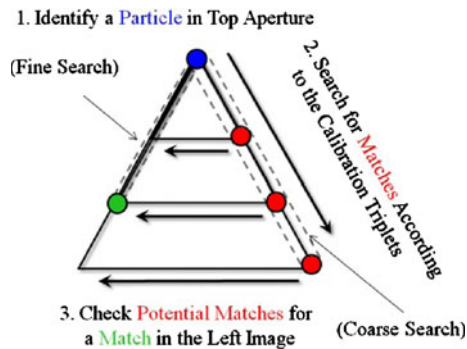
Fig. 3 Triplet search schematic diagram



Fig. 4 Unevenness of the towing tank's bottom

pixel. Since several matches may be found, a fine search is performed in finding a corresponding match from the left image. Matching particles from all three images must fit the calibration polynomial to within 0.5 pixels. These steps were performed for every particle in the field, producing a three-dimensional particle cloud at both instants. The third step was the particle tracking, which utilized a three-dimensional relaxation tracking method described in Pereira et al. (2006). This produced a randomly spaced vector field of typically 20,000 vectors. The data was then interpolated onto a regular grid through Gaussian-weighted interpolation in the fourth step.

## 2.2 Test facility

A water towing tank of $8.0^L \times 0.9^W \times 1.0^H$ m$^3$ was used for the experiments. The towing device consists of a rail car running upon the tank, precisely controlled using a computer where acceleration and speed are continuously adjustable in a range of 0–1.3 m/s (respectively m/s$^2$). Because of a minor constructional effort, the airfoil was hung up vertically with its span aligned normal to the tank's bottom. Due to the nature of this setup, the complete flow from the leading edge to the wake is observable. However, the measurement volume at the span's half point should not be altered by span-wise velocities arising from the tip-vortex' influence, with respect to the bias of two-dimensional flow and separation behavior. Hence, the gap between the airfoil's tip and the bottom of the tank had to be minimized. For this reason, the tank bottom's roughness was gauged in the run-up to the measurements. Thereby, the $X$-values were charted as soon as the height ($Z$), of the bottom, had changed about a full millimeter. The resulting curve is shown in Fig. 4, where $Z = 0$ represents the region of highest depth. The uneven bottom of the tank is clearly pointed out with the exaggerated axial ratio (approximately 400:1) and consequently, the vertical position of the airfoil was adjusted using a special adapter (see Sect. 2.3). Further direction, start- and stop-points for the towing and the locus
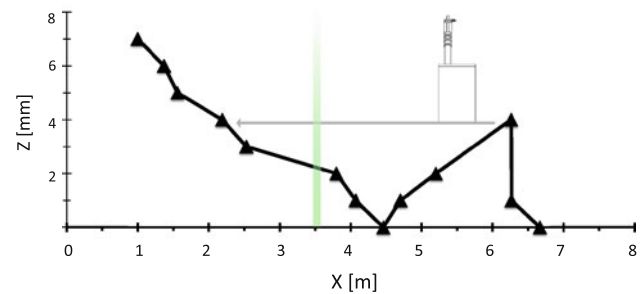
of test section were defined as shown in Fig. 4. With this configuration, it was possible to accelerate the airfoil very smoothly (0.1 m/s$^2$) to avoid vibrations of the mounting. Hence, having a towing speed of 0.2 m/s during the experiments, the acceleration/deceleration phase was finished after 0.2 m or 2.0 s. According to this, a steady airfoil flow was guaranteed in the measurement volume of the V3V system after 10 s of constant towing.

## 2.3 Construction

The constructive work included the creation of both an airfoil and a proper adapter. With respect to the speed range of the towing device, the chord length (c) of the airfoil was set to 300 mm and the width to 500 mm. It was manufactured out of massive Perspex and carefully polished afterward to avoid any surface reflections. The fully transparent nature of the airfoil allows for the measurement of the flow field on both sides of the airfoil simultaneously by using the V3V technique. This was very helpful, since the airfoil's real position could be localized in the visualization software. Obviously, the different index of refraction would introduce some parallax, but this was not important since only transition on the suction side was of fluid mechanical interest. Additionally, a concave form was milled on both sides with the intention of stabilizing the material for the cutting (especially regarding the 0.4 mm thin trailing edge) and the polishing. The airfoil was fixed on an aluminum plate and pinned with a shaft at $x/c = 0.25$, where the expected aerodynamic moments are small. The shaft was massively constructed with a diameter of 50 mm in order to make it insensitive to any vibrations. A frustum, serving as an indicator, was connected at the other end of the shaft very accurately to guarantee a true transmission of the angle of attack. The angle adjustment happened by means of a rotary table (see Fig. 5), usually used for optic applications. Thus, the airfoil could be continuously rotated around the mounting axis. A simple and precise height adjustment was realized by a three-clamp system (see Fig. 6). Using two obstructed clamps and one free clamp, the vertical and angle adjustments can
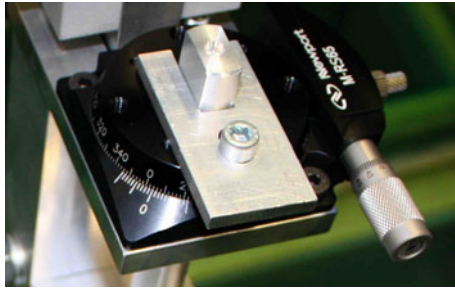
**Fig. 5** Rotary table for angle adjustment
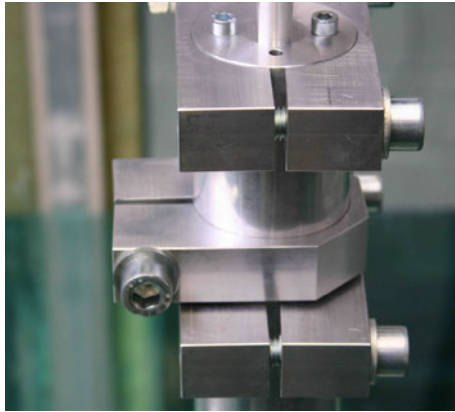


**Fig. 6** Three-clamp system

be isolated from each other. With this arrangement, the adapter is completely manageable by one person and can be adjusted easily and precisely.

### 2.4 Preliminaries

For the present experiment, a frequency-doubled New Wave YAG200-NWL dual-head pulsed Nd:YAG laser with 200 mJ at 15 Hz was applied to illuminate neutrally buoyant 50 μm polyamide (PA) particles. The laser was horizontally installed underneath the test section. Similarly to the work by Troolin and Longmire (2009), the exiting beam was expanded to a cone using two 25 mm cylindrical lenses, orientated perpendicular to each other. The resulting light cone was turned upward by a mirror (see Fig. 7). The measurement volume in the test section was $12 \times 12 \times 10$ cm$^3$. Since the amount of captured particle vectors is limited by the V3V system (see Troolin and Longmire 2009), some light-impermeable material was fixed under the channel to form the laser cone into a smaller, discrete and straight volume with the objective of increasing the spatial resolution in the region of interest (near the airfoil surface). The dimensions of the final vector fields were $10 \times 10 \times 6$ cm$^3$ with a grid spacing of 2 mm. Furthermore, the V3V camera was arranged at right angles with respect to the section walls and in proper height
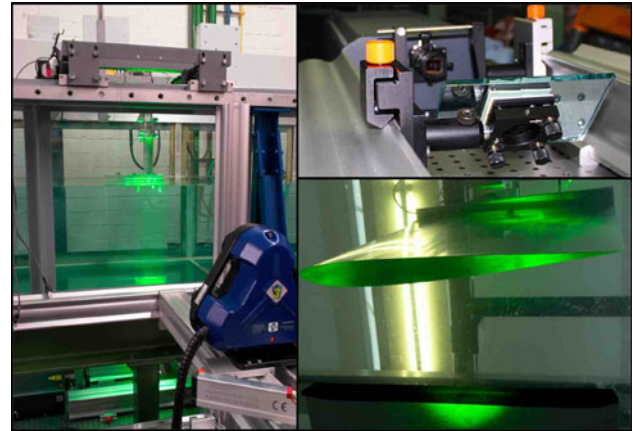


**Fig. 7** Test set-up with the V3V system

(center of measurement volume at the span's half). The adapters and the airfoil were hung up vertically at the rail car's designated precise holding fixture so that the airfoil could be lowered to reduce the gap down to less than 2 mm in the test section. This is important since the tip-vortex rising from the pressure gradient along the tip edge would affect the flow in the span-wise direction and influence the transition scenario. Previously, the 50 μm PA powder was compared with 10 μm glass hollow spheres. Both of them showed a negligible sinking speed (complete sedimentation after 24 h), which is very important due to the fact that the fluid is completely stagnant before each measurement. Additional analyses have shown that both types of seeding do not clump up, but the 10 μm tracers proved to be too small for the tracking algorithm of the V3V system, hence they were not used. The PA tracers were premixed to create a homogeneous suspension. Due to the complete filling of the tank's volume, a frequent addition of seeding-suspension was necessary during the experiments since the seeding disperses due to the towing of the target. Note that the addition and suspension of PA tracer mixture took some time to homogenize, or diffuse, until the appropriate density for 3D particle tracking was reached in the measurement volume. This can be estimated by the amount of valid particle vectors after a fast evaluation with the systems internal software (some minutes).

## 3 Results

The measurements were performed at $\alpha = 4°$ and $Re = 60{,}000$, which corresponds to a free-stream velocity of $u_\infty = 0.2$ m/s. As a reference, $\alpha = 8°$ was investigated as well. For the final evaluation process, all visualizations were produced with Tecplot. Hence, for a proper evaluation, the data had to be transformed to the fluid mechanical coordinate system by adding the towing speed. Moreover,

the vector fields recorded at different times were shifted according to $\Delta x = u_\infty / f$, where $f$ is the camera frame rate (7.25 Hz).

## 3.1 Uncertainty of the arrangement

The sources of uncertainty in the V3V technique are primarily associated with the accurate identification of the particle locations. The sensor arrangement allows for the determination of accurate spatial locations up to an uncertainty of $\pm 20$ μm in $X$ and $Y$, and $\pm 80$ μm in $Z$, as determined by the solid motion of a plate with seeding particles on the surface. The uncertainty in the timing resolution was negligible, so that in the current experiment, the uncertainty in absolute velocity, $(u/u_\infty, v/u_\infty)$, was approximately $\pm 2.5\%$. But since the seeding was frequently added only to the measurement volume, the remaining volume in front of the test section showed a very low seeding concentration in regions where the airfoil approaches and the boundary layer develops. This is supposed to be the main reason for the lack of tracers in the boundary layer, which explains why the near-wall region was not resolved during the experiments.

## 3.2 Disturbed airfoil flow

In order to examine the three-dimensional coherent vortex structures, the free-stream flow should be two-dimensional and a bias error due to the water surface, the starting-vortex and the gap flow should be neglected. Since the water is at rest and the towing speed is very low (0.2 m/s), the water surface's influence is negligible. But by counter-rotating to the airfoil's circulation, the starting-vortex has got an immediate effect on the flow just after the initial motion of the airfoil. The tests should consider the size, as well as the dislocation, of the starting-vortex whose effect is strongly related to the working principle of a towing tank. Therefore, the airfoil was properly positioned in the measurement volume with the focus on its trailing edge. The acceleration was set to 1.0 m/s$^2$, since it has been shown that accelerations less than 1.0 m/s$^2$ do not suffice for a clear starting-vortex. This means that the airfoil is accelerated for only 0.2 s or 2 cm (0.06 c). Finally, the influence due to the starting-vortex according to the Biot-Savart law was negligible as well as the distance between the starting point of the airfoil and the measurement section was above 2 m for the present experiments. On the other hand, the tip-vortex may have a negative effect on the transition for two reasons: (1) due to the span-wise flow component induced by the gap flow, the consideration of a two-dimensional flow might not be valid and a cross-flow instability might be superimposed on the T-S instability and (2) due to the deceleration of the streamwise motion in the corner-vortex,

the free-stream velocity is increased as a consequence of continuity. This may stabilize the flow and must be investigated as well. To study these effects, the airfoil was lifted about 10 cm from the bottom so the measurement volume (V3V camera) was properly positioned and the tip-vortex could take effect. Now, the steady airfoil flow was examined, which only has a tip-vortex in the measurement volume, since the starting-vortex remains at the airfoil's starting position. As discussed, the tip-vortex would induce a velocity in span-wise direction, which increases the total velocity. This could heavily change the transition scenario. In the following the investigations for $\alpha = 8°$ were found to be good at presenting the tip-vortex, due to the lift coefficient, which is at least 60% larger than at $\alpha = 4°$. The tip-vortex' temporal-spatial development is shown in Fig. 8. For this purpose, iso-surfaces of a negative second Eigen value $\lambda_2$ (by Jeong and Hussain 1995) were plotted and contoured with the normalized wall-parallel swirling strength. The tip-edge is located at $z = 0$. As mentioned before, all snapshots of a single measurement, recorded at successive times, were first shifted and overlaid. Because of this, overlapping structures might be interpreted as new coherent ones. Nevertheless, one recognizes the tip-vortex' history as expected. All in all, the tip-vortex' swirling motion causes a strong boundary layer mixing nearby. Furthermore, span-wise velocities are induced as shown in Fig. 9. There, the distribution of the span-wise velocity component of five single snapshots near the airfoil is depicted. The velocity sections are inclined about the value of $\alpha$, just as the data grid. Whereas, at $t_0$ the flow of both the suction and the pressure side gets distracted toward the edge, the span-wise velocities induced by the tip-vortex are dominant at $t_0 + 0.414$ s. Until $t_0 + 1.242$ s, the vortex-influence moves almost completely to the suction side and gains further momentum. At $t_0 + 1.379$ s purple $\lambda_2$-iso-surfaces, 3D vectors along the section planes and streamlines were additionally inserted to mark the tip-vortex, which has reached its maximum strength running off with the mainstream from this point. It is important to conclude
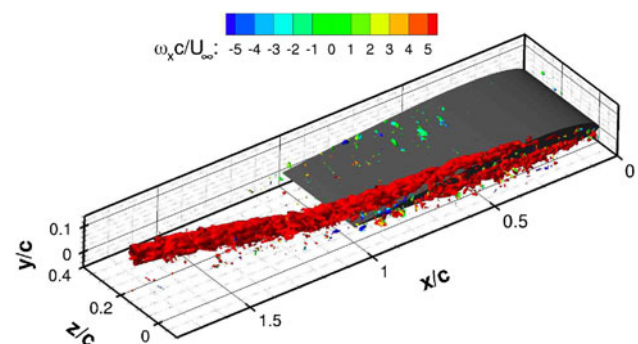


**Fig. 8** Development of a tip-vortex for $\alpha = 8°$ and $Re = 60,000$; $\lambda_2$-iso-surfaces flooded with normalized stream-wise vorticity

**Fig. 9** Temporal-spatial development of the span-wise velocity component for $\alpha = 8°$ and $Re = 60,000$
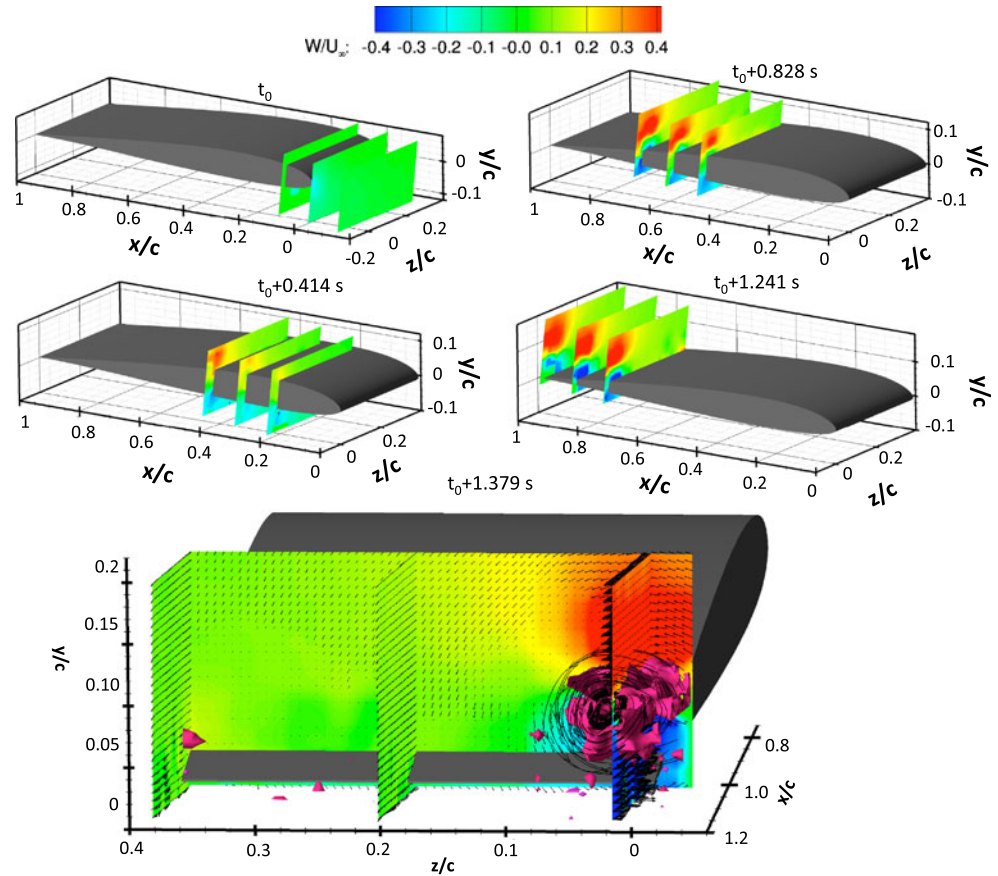


that the span-wise affected area is already quite small ($z < 0.2$ c). As an additional reduction takes place for smaller angles of attack ($\alpha = 4°$) and tiny gaps ($\leq 2$ mm), the effect of the gap flow on the transition process at the centerline can be neglected for this experiment. Afterward, the influence becomes negligible by lowering the airfoil, reducing the strength of the tip-vortex by decreasing the gap and changing $\alpha$ to $4°$. One would expect a LSB similar to the one shown in Fig. 1 under these conditions.

## 3.3 Undisturbed airfoil flow

### 3.3.1 Vortex shedding

The incident flow near the span's mid-point is two-dimensional. As a consequence, three-dimensional coherent vortex structures can be distinguished. Figure 10 shows the instant streamwise velocity distribution. The main section plane is at $y = 0.05$ c. Due to the fact that the near-wall region was not fully resolved due to the lack of seeding (see Sect. 3.1), the random particle vectors were additionally plotted (black dots) to verify the credibility of the data. This is necessary since an interpolated vector replaces every vacancy. However, downstream of $x/c = 0.7$, there are several areas of a decreased streamwise velocity magnitude

($u/u_\infty = 0.5$) also found in the literature (i.e. Burgmann et al. 2007; Hain and Kähler 2005; Zhang et al. 2008). With the aid of $\lambda_2$-iso-surfaces, the corresponding vortices could be located as well. Their cores have an approximate size of $0.04^x \times 0.04^y \times 0.06^z$ c$^3$. As further measurements at $Re = 60,000$ and $\alpha = 4°$ confirmed, these vortices shed more or less in a regular chessboard pattern. In Fig. 11, the vortices are flooded by contours of the normalized swirling strength. Whereas the normalized span-wise vorticity $\omega_z c/u_\infty$ is uniformly negative, both $\omega_x c/u_\infty$ and $\omega_y c/u_\infty$ are distributed asymmetrically on the edge regions of the vortices. This underlines the three-dimensional character of these structures and stands in interdependency with a regular distribution of sources and sinks, which is shown in detail in Fig. 12. The snapshot displays the section-normal view of Fig. 11 (vortices included), but this time the regular vector field along the section plane is shown. Since the regular vectors indicate the real instant flow behavior (towing speed $u_\infty = 0.2$ m/s$^2$ was not yet added to the vector field), the sources and sinks look a little unusual. It can be stated, however, that a source is located upstream of a vortex and a sink downstream of it. Hain et al. (2009) also recorded the presence of sources and sinks associated with the presence of a vortex, though in the opposite order. As a consequence, the detected vortices seem to be different

**Fig. 10** Distribution of $u/u_\infty$-magnitude and random particle vectors (*black dots*) at $\alpha = 8°$ and $Re = 60{,}000$; additionally with $\lambda_2$-iso-surfaces (*right*)
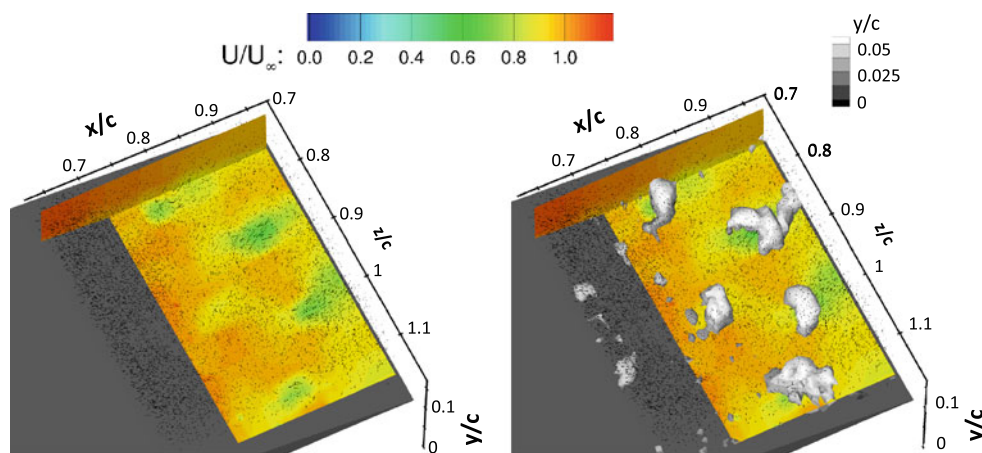


**Fig. 11** Dynamical properties of the shed vortices; planes with $u/u_\infty$-magnitude and $\lambda_2$-iso-surfaces flooded with the different normalized vorticities for $\alpha = 4°$ and $Re = 60{,}000$
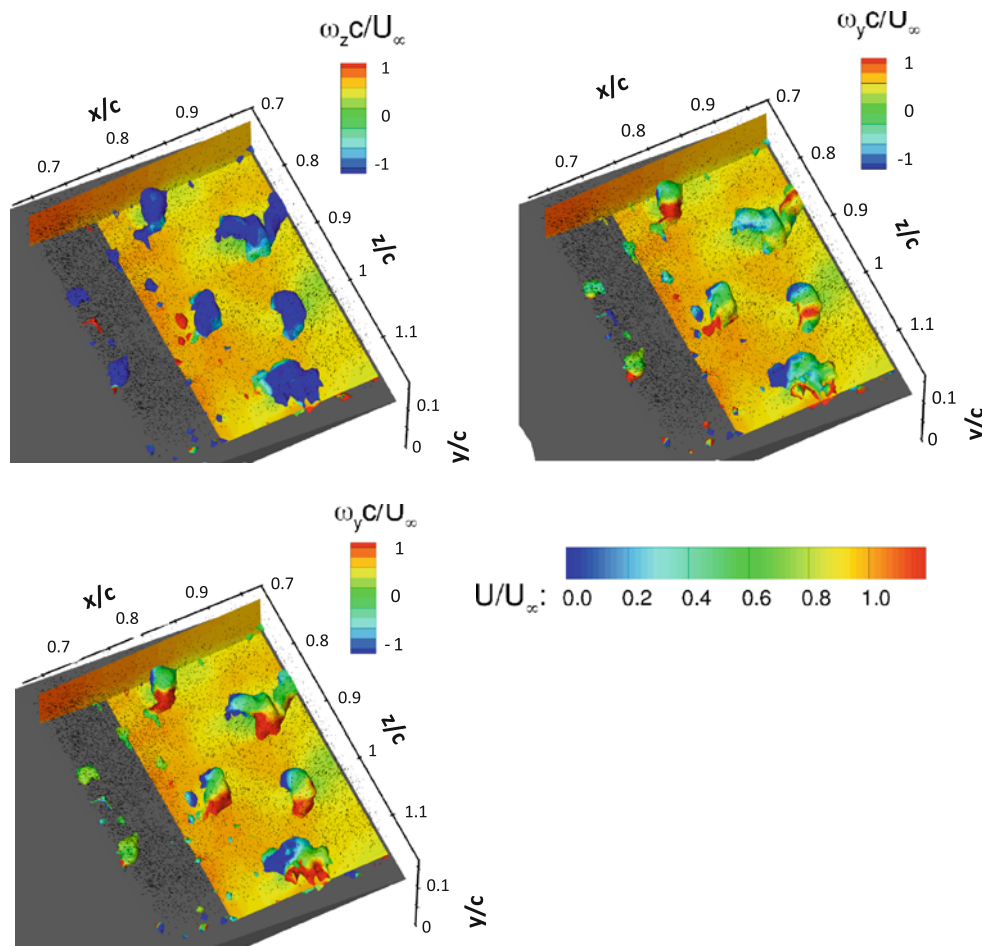
from the C-shape vortex by Burgmann et al. (2007) or the ones found by Hain and Kähler (2005). Nevertheless, it must be mentioned that their findings are not in conflict with the present results, regarding the fact that they investigated regions much closer to the airfoil's surface (below $y = 0.05$ c). However, the vortices show similarities with the arc-like structures first observed by Zhang et al. (2008), even though they have to be time-resolved for a better judgment.

### 3.3.2 Vortex evolution

Figure 13 shows the temporal-spatial development of the known group of vortices. For this purpose, the vortex cores were identified with $\lambda_2$-iso-surfaces and flooded by the $y$-magnitude to indicate their 3D position. Furthermore, asymmetric iso-surfaces of the normalized wall-normal vorticity were added to distinguish between individual
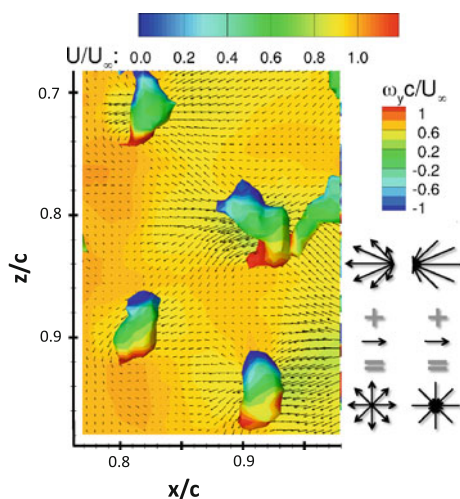
**Fig. 12** Distribution of $u/u_\infty$-magnitude at $\alpha = 4°$ and $Re = 60,000$ with regular grid vectors at $y = 0.05$ c; $\lambda_2$-iso-surfaces flooded with wall-normal vorticity

vortices. At $t_0$, the structures A to E are located in the same plane. Thus, vortices A, C and E are equally spaced at a distance of 0.15 c from each other along a fictitious spanwise line. Having a similar distance among each other, the vortices B and D are displaced approximately 0.1 c in the downstream direction and diagonally shifted. Up to $t_0 + 3\Delta t$ ($\Delta t = 0.138$ s), all vortices have reached their maximum size and moved slightly downstream. Furthermore, a new larger structure F has slid in the range. In the meantime, C approached D, but until $t = t_0 + 10\Delta t$, it descended out of the measurement volume in the $y$-direction. During this process, the resting vortices moved downstream, without altering their positions among each other in the surface-parallel plane. Considering the convection velocity and the vortices' spacing, one can estimate the shedding frequency. Comparing the constellation of the first and the fourth frame ($t_0$ and $t_0 + 3\Delta t$), vortex A, for instance, has moved approx. 0.18 c (54 mm). With a camera frame rate of $f = 7.25$ Hz, the normalized convection velocity is $u_C/u_\infty = 0.65$. Similar values were found by Hain (2009). This corresponds to a frequency of 4.3 Hz for the vortex shedding if i.e. the distance between vortex A and B is used. Otherwise, if only a very thin volume ($z < 0.1$ c) was captured, the shedding frequency would appear half as large (2.2 Hz), since only every second vortex would be detected. This computed value for the frequency does not correspond to the reported values in the existing literature, since it is possibly related to a very low turbulence level. As a reference, the vortex shedding at $\alpha = 8°$ was examined, see Fig. 14. The visualization is similar to Fig. 13. With increasing $\alpha$, the bubble becomes shorter and the corresponding vortices could already be detected at $x = 0.5$ c. Furthermore, probably due to the faster transition, there are more of them, and they are once again

diagonally shifted among each other though the chessboard pattern cannot be seen clearly. The pictured vortices keep their identity and their relative positions among each other in the $x$–$z$-plane. As time passes, the smaller vortices move towards the model, whereas the large-scale structures keep their positions in the mainstream flow. The convection velocity is a little higher than at $\alpha = 4°$, since most of the vortices move approximately 0.2 c in $2\Delta t$. Regarding the vortices grayscales (at $\alpha = 4°$ and $\alpha = 8°$), the large-scale structure extends further in the $y$-position. Yet, its vorticities seem to be similar to the ones of the smaller vortices, which is why a high degree of detail is presented in Fig. 15. The $\lambda_2$-iso-surface was flooded with the normalized spanwise swirling strength, and the particle vectors were inserted. Here, the $y$- and $z$-extensions (approximately 0.12 c) are obvious. The volume below $y = 0.05$ c was blocked from laser illumination due to the light impermeable material, originally fixed under the channel to increase the spatial resolution. Hence, iso-surfaces are not shown below this level since they all descend from interpolated vectors with replacement characters. The credibility of the iso-surfaces was again checked by also displaying the random particle vectors. Consequently, no statement about this vortex' topology can be given, except that it has an arc- or rather a $\Lambda$-shape in the valid range with two counter-rotating vortex arms. These structures were also observed by Watmuff (1999), Zhang et al. (2008) and Burgmann and Schröder (2008), though they were smaller and much closer to the airfoil's surface. It can be stated that the more frequently detected and smaller vortices, with respect to their vorticity, are also arc-like structures, which is in good agreement with the flow behavior (sources and sinks) shown in Fig. 12.

## 4 Conclusions

The objective of this study was the quantitative investigation of unsteady 3D coherent vortex structures arising from the point of reattachment of an LSB using the innovative V3V technique. The experiments were performed in a water towing tank at $Re = 60,000$ and $\alpha = 4°$ to minimize the influence of the turbulence level on the transition. First of all, the effect of the starting- and tip-vortex on the two-dimensionality of the flow and the coherent structures on the center of the airfoil was assessed. Consequently, the influences were minimized by the test set-up where a two-dimensional incident flow was investigated. Thereby, at 70 % of the chord, a group of arc-like vortices was detected, having a regular order (chessboard) and corresponding to a regular distribution of sources and sinks as observed at larger turbulence levels in water tunnels. Thus, it can be concluded that these structures are not fixed by the

**Fig. 13** Development of the shed vortices at $\alpha = 4°$ and $Re = 60{,}000$; $u/u_\infty$-planes, $\lambda_2$-iso-surfaces flooded with $y$-position and $\omega_y c/u_\infty$-iso-surfaces
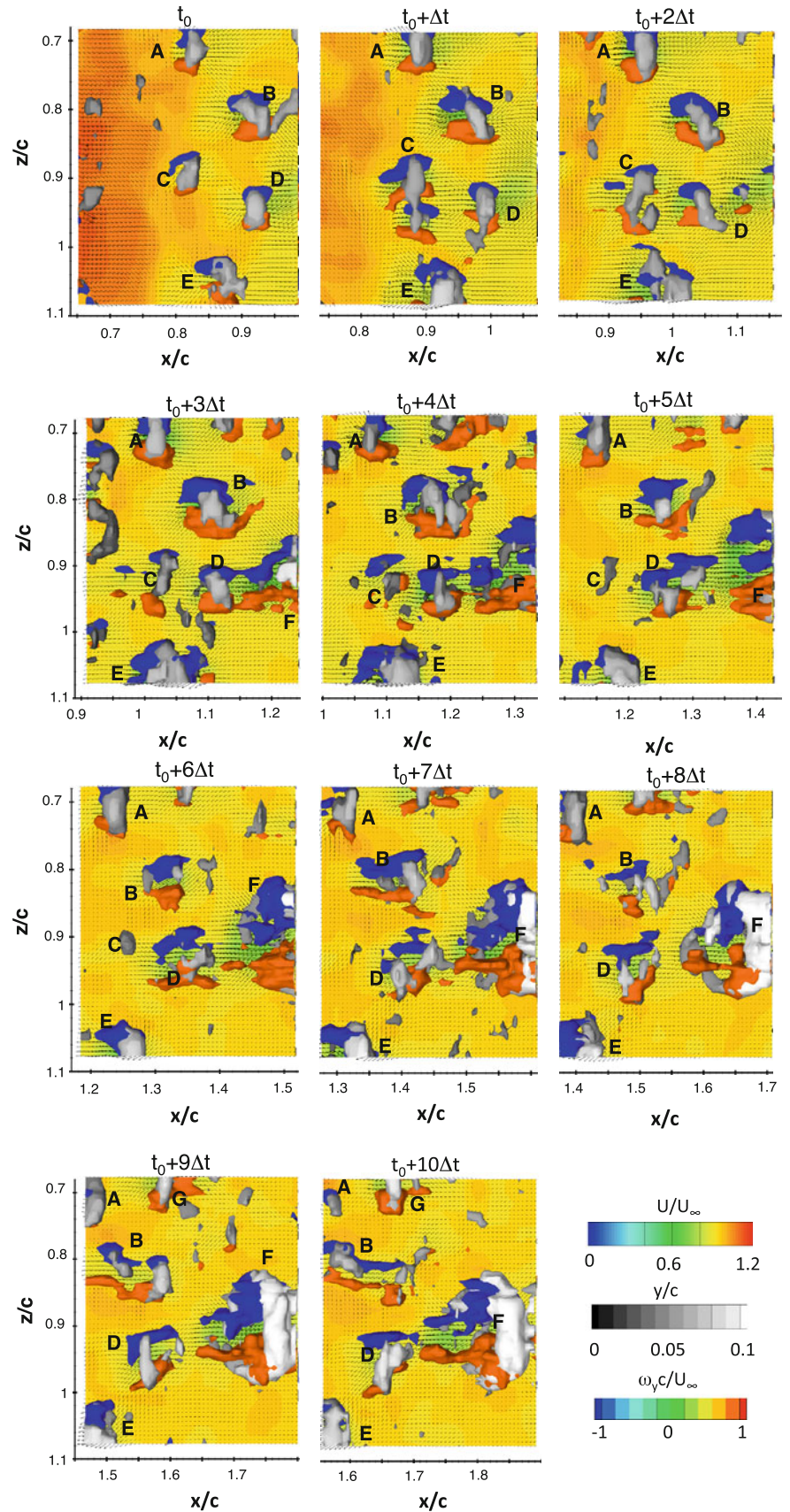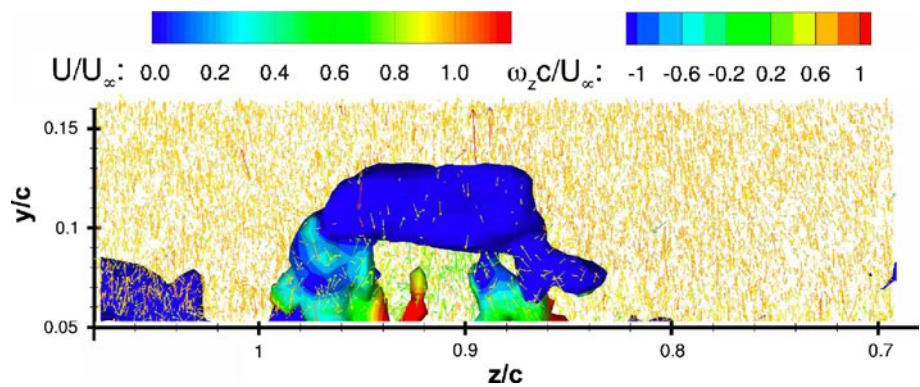
**Fig. 14** Development of the shed vortices at $\alpha = 8°$ and $Re = 60{,}000$; $u/u_\infty$-planes, $\lambda_2$-iso-surfaces flooded with $y$-position and $\omega_y c/u_\infty$-iso-surfaces
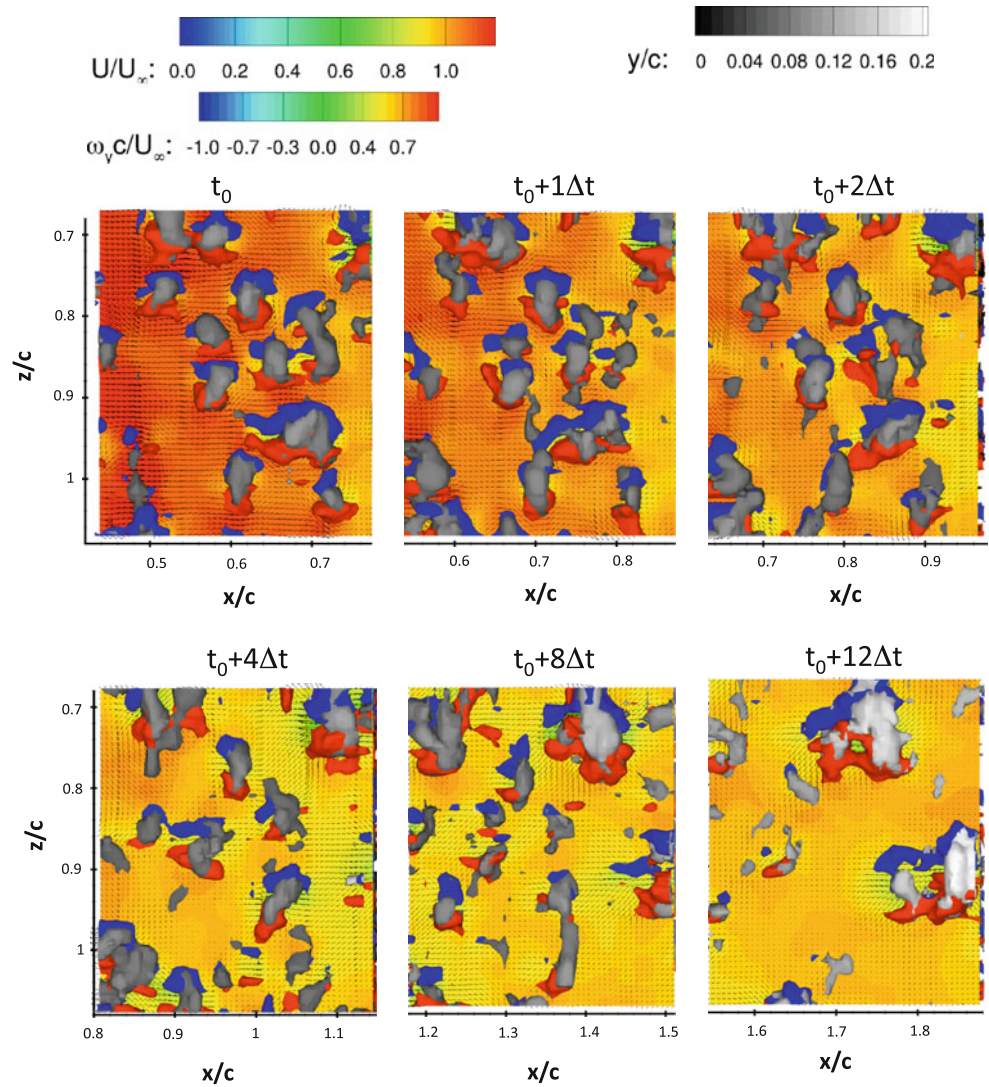


**Fig. 15** Large-scale structure at $x = 1.87$ c ($\alpha = 4°$ and $Re = 60{,}000$); particle vectors flooded with $u/u_\infty$-magnitude and $\lambda_2$-iso-surfaces flooded with the normalized span-wise vorticity magnitude



free-stream-turbulence. The shed vortices' further development was time-resolved. Additionally, a large-scale vortex, which extended into the illuminated volume, was detected. In the valid range, it is arc-like and possesses two counter-rotating vortex-arms, but the dynamics of its structure, which extended outside of the illuminated volume, were not resolved. Nevertheless, this study shows that 3D Λ-shape coherent structures do not only exist in the reattachment region of an LSB. They actually keep their body structure to the far wake of the airfoil. Furthermore, they can be regularly ordered if there is a low-turbulent environment.

# References

Alam M, Sandham ND (2000) Direct numerical simulation of "Short" laminar separation bubbles with turbulent reattachment. J Fluid Mech 410:1–28

Burgmann S, Dannemann J, Schröder W (2007) Time-resolved and volumetric PIV measurements of a transitional separation bubble on an SD7003 airfoil. Exp Fluids 44: 609–622

Burgmann S, Schröder W (2008) Investigation of the vortex induced unsteadiness of a separation bubble via time-resolved and scanning PIV measurements. Exp fluids 45: 675–691

Gaster M (1966) The structure and behaviour of laminar separation bubbles. AGARD CP-4, pp 813–854

Hain R (2009) Untersuchung der Dynamik laminarer Ablöseblasen mit der zeitaufgelösten particle image velocimetry. Ph.D. Thesis, Technical University Braunschweig

Hain R, Kähler CJ (2005) Advanced evaluation of time-resolved PIV image sequences. In: 6th International symposium on particle image velocimetry, Pasadena, 21–23 September

Hain R, Kähler CJ, Radespiel R (2009) Dynamics of laminar separation bubbles at low-Reynolds number aerofoils. J Fluid Mech 630:129–153

Horton H (1968) Laminar separation bubbles in two and three-dimensional incompressible flow. Ph.D. Thesis, Department of aeronautical engineering, Queen Mary College/University of London

Jeong J, Hussain F (1995) On the identication of a vortex. J Fluid Mech 285:69–94

Ol MV, Hanff E, McAuliffe B, Scholz U, Kähler CJ (2005) Comparison of laminar separation bubble measurements on a low Reynolds number airfoil in three facilities. In: 35th AIAA fluid dynamics conference and exhibit, Toronto, 6–9 June

Pauley LL, Moin P, Reynolds WC (1990) The structure of two-dimensional separation. J Fluid Mech 220:397–411

Pereira F, Gharib M, Dabiri D, Modarress D (2000) Defocusing digital particle image velocimetry: a 3-component 3-dimensional DPIV measurement technique. Application to bubbly flows. Exp Fluids Suppl S78–S84

Pereira F, Stuer H, Graff EC, Gharib M (2006) Two-frame 3D particle tracking. Meas Sci Technol 17:1680–1692

Spalart P, Strelets M (2000) Mechanisms of transition and heat transfer in a separation bubble. J Fluid Mech 403:329–349

Troolin DR, Longmire EK (2009) Volumetric velocity measurements of vortex rings from inclined exits. Exp Fluids 48:409–420

Watmuff JH (1999) Evolution of a wave packet into vortex loops in a laminar separation bubble. J Fluid Mech 397:119–169

Willert CE, Gharib M (1992) Three-dimensional particle imaging with a single camera. Exp Fluids 12:353–358

Yang Z, Voke PR (2001) Large-Eddy simulation of a boundary-layer separation and transition at a change of surface curvature. J Fluid Mech 439:305–333

Zhang W, Hain R, Kähler CJ (2008) Scanning PIV investigation of the laminar separation bubble on a SD7003 airfoil. Exp Fluids 45:725–743